Binuclear Biphenyl Organogold(III) Complexes: Synthesis, Photophysical and Theoretical Investigation, and Anticancer Activity

Valerio Giuso, Jeannine Yang, Jérémy Forté, Héloïse Dossmann, Chantal Daniel, Christophe Gourlaouen, Matteo Mauro, Benoît Bertrand

Chemistry Europe
European Chemical Societies Publishing

WILEY VCH

Excellence in Chemistry Research

Announcing our new flagship journal

- Gold Open Access
- Publishing charges waived
- Preprints welcome
- Edited by active scientists

Meet the Editors of *ChemistryEurope*

Luisa De Cola
Università degli Studi di Milano Statale, Italy

Ive Hermans
University of Wisconsin-Madison, USA

Ken Tanaka
Tokyo Institute of Technology, Japan

ChemPlusChem

Research Article
doi.org/10.1002/cplu.202300303

Chemistry Europe
European Chemical Societies Publishing

www.chempluschem.org

Special Collection

Binuclear Biphenyl Organogold(III) Complexes: Synthesis, Photophysical and Theoretical Investigation, and Anticancer Activity

Valerio Giuso[+],[a] Jeannine Yang[+],[b] Jérémy Forté,[b] Héloïse Dossmann,[b] Chantal Daniel,[c] Christophe Gourlaouen,[c] Matteo Mauro,*[a] and Benoît Bertrand*[b]

A series of four binuclear complexes of general formula [(C^C)Au(Cl)(L^L)(Cl)Au(C^C)], where C^C is 4,4′-diterbutylbiphenyl and L^L is either a bridging diphosphine or 4,4′-bipyridine, are synthetized with 52 to 72% yield and structurally characterized by X-ray diffraction. The use of the chelating 1,2-diphenylphosphinoethane ligand in a 1:2 (P^P):Au stoichiometry leads to the near quantitative formation of a gold double-complex salt of general formula $[(C^C)Au(P^P)][(C^C^)AuCl_2]$. The compounds display long-lived yellow-green phosphorescence with λ_{em} in the range of 525 to 585 nm in the solid state with photoluminescence quantum yields (PLQY) up to 10%. These Au^{III} complexes are tested for their antiproliferative activity against lung adenocarcinoma cells A549 and results show that compounds **2** and **5** are the most promising candidates. The digold salt **5** shows anticancer activity between 66 and 200 nM on the tested cancer cell lines, whereas derivative **2** displays concentration values required to reduce by 50% the cell viability (IC_{50}) between 7 and 11 μM. Reactivity studies of compound **5** reveal that the $[(C^C)Au(P^P)]^+$ cation is stable in the presence of relevant biomolecules including glutathione suggesting a structural mechanism of action.

Introduction

The organometallic chemistry of Au^{III} has been developing exponentially in the last two decades.[1–5] In particular, the use of cyclometalated ligands that possess at least a M–C and a M-heteroatom bond enables the stabilization of the Au^{III} center, opening the way to various structures and applications.[6,7] Complexes with C^N,[8–12] N^N^C,[13] C^C^N[14] and C^N^C[15–20] cyclometalating ligands have found applications for their intriguing photoluminescence and anticancer activities.

Among all polydentate ligands associated with cyclometalated Au^{III} scaffolds, diphosphines can be found in a large panel of structures reported for their anticancer properties. Some relevant examples are displayed in Figure 1. Notably, dicationic binuclear compounds featuring C^N^C–Au^{III} complexes with diphenylphosphinoalkane bridges were shown to have sub-μM activities on hepatocarcinoma cells and tumors,[21,22] while C^N–Au^{III} scaffolds with chelating diphosphines led to the development of $[(C^N)Au(P^P)]^{2+}$ mononuclear dications with

[a] V. Giuso,[+] Dr. M. Mauro
Institut de Physique et Chimie des Matériaux de Strasbourg UMR 7504
Université de Strasbourg & CNRS
23 rue du Loess, 67034 Strasbourg (France)
E-mail: mauro@unistra.fr

[b] J. Yang,[+] J. Forté, H. Dossmann, Dr. B. Bertrand
Institut Parisien de Chimie Moléculaire UMR 8232
Sorbonne Université
4 Place Jussieu, 75005, Paris (France)
E-mail: benoit.bertrand@sorbonne-universite.fr

[c] Dr. C. Daniel, Dr. C. Gourlaouen
Institut de Chimie de Strasbourg, UMR 7177
Laboratoire de Chimie Quantique
Université de Strasbourg & CNRS
4 rue Blaise Pascal, 67081 Strasbourg (France)

[+] These authors contributed equally to this work.

Supporting information for this article is available on the WWW under https://doi.org/10.1002/cplu.202300303

Special Collection Part of a Special Collection on Gold Chemistry.

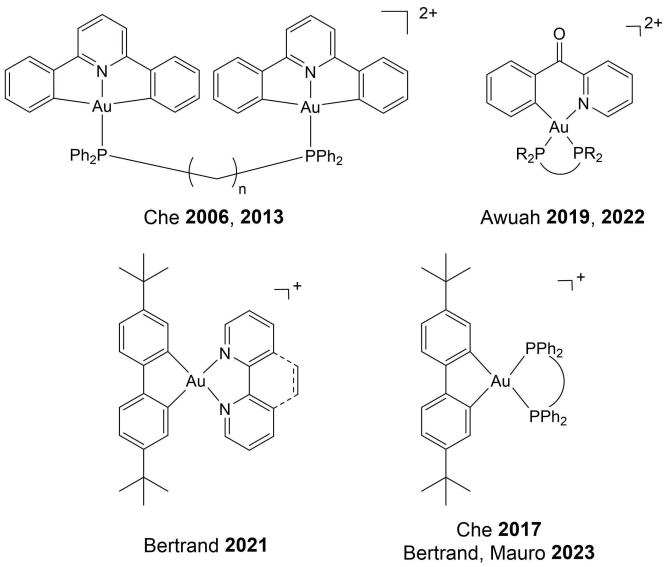

Figure 1. Structures of the Au^{III} complexes with cyclometalating C^N^C, C^N and C^C scaffolds and either diimine or diphosphine ligands reported to date for anticancer and photoluminescence properties.

very high *in vitro* and *in vivo* cytotoxicity due to their high antimitochondrial activity.[23,24]

In the last decade, the use of biphenyl C^C chelates has been applied to Au^{III} chemistry that yielded complexes not only interesting for fundamental gold chemistry,[25] but also with applications in various areas such as catalysis[26,27] and photoluminescence.[28,29] In particular, some of us reported on the anticancer potential of $[(C^C)Au(N^N)]^+$ complexes (Figure 1), which were shown to be redox stable in the presence of the cellular reducing agent glutathione (GSH).[30] Replacement of the diimine N^N ligand by chelating diphosphines led to a series of $[(C^C)Au(P^P)]^+$ complexes (Figure 1), which displayed intense solid state luminescence in the green range.[29,31] Taking advantage of their high redox and thermal stability this latter family of complexes were successfully applied in the fabrication of the first Au^{III}-based light-emitting electrochemical cells (LECs).[31]

Considering the larger panel of accessible structures offered by the [(C^C)Au] scaffold, we report here on the preparation and characterization of neutral binuclear derivatives using either chelating or non-chelating diphosphine ligands as well as ditopic 4,4′-bipyridine. The photophysical properties of the compounds were studied in solution and in solid state and their behaviour further rationalized with the help of computational investigation at (time-dependent) density functional theory (TD-DFT) level. Finally, the compounds were screened for their antiproliferative properties against human lung adenocarcinoma cells enabling the identification of the most promising candidates, which were studied on a larger panel of cancer and non-cancer cells.

Results and Discussion

When non-chelating ligands such as 4,4′-bipyridine, *trans*-1,2-*bis*(diphenylphosphino)ethylene, diphenylphosphinoacetylene and 1,4-bis(diphenylphosphino)benzene were employed in a 1:2 ratio with respect to the [(C^C)AuCl] precursor, we observed the quantitative formation of the corresponding neutral binuclear compounds **1**–**4**. The general synthetic pathway is displayed in Scheme 1.

The formation of the binuclear complexes **1**–**4** was assessed by ^1H and $^{31}P\{^1H\}$ NMR spectroscopies. Indeed, ^1H NMR spectrum of **1**, **2** and **3** shows a doublet of doublets at $\delta = 8.48$, 8.43 and 8.37 ppm, respectively, which corresponds to H^{11} coupled with the phosphorous atom in the absence of aromatic shielding due to the presence of the chlorido ligand as previously observed for [(C^C)Au(L)Cl] complexes.[28] Moreover, the signal of the $^{31}P\{^1H\}$ appears at $\delta = 42.1$, 34.7 and 20.0 ppm for complexes **1**, **2** and **3**, respectively. For compound **1** bearing the non-chelating 1,4-*bis*(diphenylphosphino)benzene, the $^{31}P\{^1H\}$ signal is shielded by 10 ppm compared to the cationic complexes with the chelating 1,2-*bis*(diphenylphosphino)benzene ligand[31] (fig. 1) suggesting a less Lewis acidic character of the Au^{III} center, in good agreement with the charge-neutral nature of the compound. Complex **4** appeared poorly soluble in most organic solvents. Nevertheless,

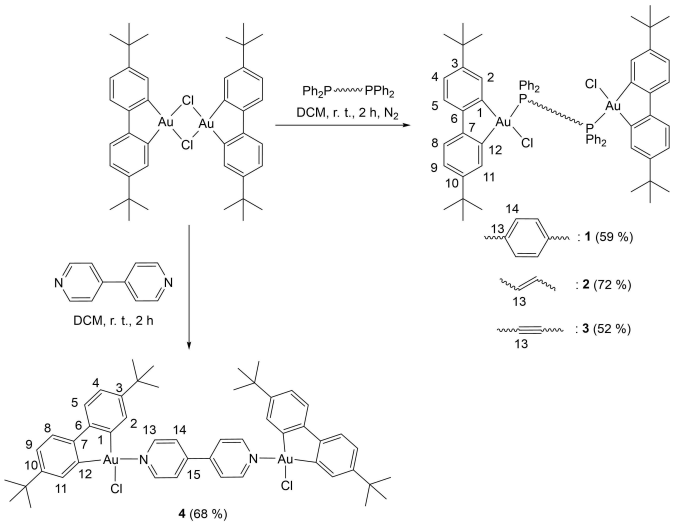

Scheme 1. Synthesis of binuclear complexes **1**–**4**.

it was possible to record an ^1H NMR spectrum in CD_2Cl_2 that resembles the spectrum of the monomeric analog [(C^C)Au(pyridine)Cl] with the signals of H^2 and H^{11} appearing at $\delta = 6.49$ and 8.16 ppm, respectively.[28]

On the other hand, when the same reaction was carried out using 1,2-*bis*(diphenylphosphino)ethane, (dppe), the $^{31}P\{^1H\}$ spectrum of the obtained product showed a signal at $\delta =$ 59.7 ppm matching exactly with the signal of the phosphine in the corresponding cationic $[(C^C)Au(P^P)]^+$ complex.[31] Moreover, on the ^1H spectrum, signals corresponding to the cationic $[(C^C)Au(P^P)]^+$ complex could be observed, especially H^2 at 7.28 ppm. The remaining signals appeared to be due to a [(C^C)Au] fragment with symmetrical counterligands. The signal of H^9 appeared as a doublet with no phosphorous coupling at $\delta = 8.30$ ppm, suggesting the presence of a $[(C^C)AuCl_2]^-$ anion.[32] Altogether, these data suggest that the chelating dppe ligand formed the chelate instead of acting as a bridging ligand even when the reaction was carried out in a 1:2 molar ratio of (P^P):Au, respectively, leading to the formation of the bis-organogold complex salt **5** in very good yield (Scheme 2).

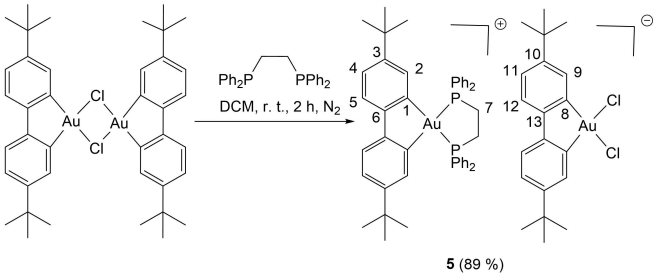

Scheme 2. Synthesis of the digold double-complex salt **5**.

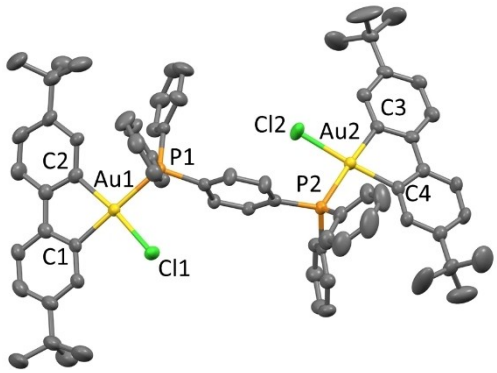

Figure 2. Crystal structure of complex **1**. Ellipsoids set at 50% probability. Hydrogen atoms and *i*$^{-}$PrOH molecules have been omitted for clarity. Selected bond distances [Å] and angles [°] measured at 200 K: Au_1–Cl_1 2.3730(12), Au_1–P_1 2.3969(12), Au_1–C_2 2.070(5), Au_1–C_1 2.064(5), Au_2–Cl_2 2.3635(13), Au_2–P_2 2.4067(12), Au_2–C_4 2.065(5), Au_2–C_3 2.069(5), Cl_1–Au_1–P_1 85.50(4), P_1–Au_1–C_2 100.16(15), C_2–Au_1–C_1 80.5(2), C_1–Au_1–Cl_1 93.84(14), Cl_2–Au_2–P_2 89.03(4), P_2–Au_2–C_4 96.45(14), C_4–Au_2–C_3 80.82(19), C_3–Au_2–Cl_2 93.68(14).

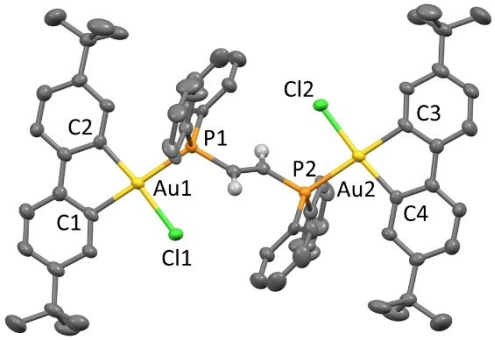

Figure 3. Crystal structure of complex **2**. Ellipsoids set at 50% probability. Only hydrogens of the bridge have been shown for clarity. Selected bond distances [Å] and angles [°] measured at 200 K: Au_1–Cl_1 2.3715(15), Au_1–P_1 2.4366(14), Au_1–C_2 2.074(6), Au_1–C_1 2.088(6), Au_2–Cl_2 2.3720(13), Au_2–P_2 2.4226(14), Au_2–C_4 2.054(5), Au_2–C_3 2.074(6), Cl_1–Au_1–P_1 86.89(5), P_1–Au_1–C_2 98.39(16), C_2–Au_1–C_1 81.0(2), C_1–Au_1–Cl_1 93.56(18), Cl_2–Au_2–P_2 88.29(5), P_2–Au_2–C_4 97.10(16), C_4–Au_2–C_3 81.1(2), C_3–Au_2–$Cl_2$93.45(15).

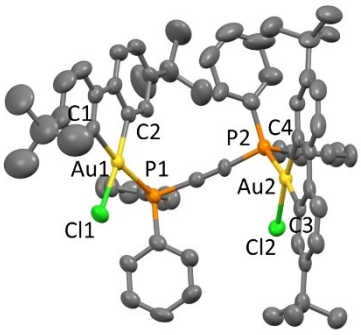

Figure 4. Crystal structure of complex **3**. Ellipsoids set at 50% probability. Hydrogen atoms have been omitted for clarity. A PLATON SQUEEZE procedure is applied. Selected bond distances [Å] and angles [°] measured at 200 K: Au_1–Cl_1 2.3570(14), Au_1–P_1 2.3948(13), Au_1–C_2 2.060(6), Au_1–C_1 2.087(6), Au_2–Cl_2 2.3792(12), Au_2–P_2 2.4232(14), Au_2–C_4 2.060(6), Au_2–C_3 2.059(6), Cl_1–Au_1–P_1 89.77(5), P_1–Au_1–C_2 95.90(18), C_2–Au_1–C_1 81.0(3), C_1–Au_1–Cl_1 93.7(2), Cl_2–Au_2–P_2 81.94(5), P_2–Au_2–C_4 103.38(19), C_4–Au_2–C_3 81.1(2), C_3–Au_2–Cl_2 93.85(16).

X-ray diffraction analysis

Single crystals suitable for X-ray diffraction were grown by slow evaporation of a DCM/*i*-PrOH or DCM/MeOH solution of the complexes, and the corresponding crystal structures are depicted in Figures 2–6.

For all the complexes including the digold salt **5**, the crystallographic data confirmed the expected structures. The crystal structures of the dimeric complexes **1**–**4** show the expected tetracoordinated square-planar geometry of Au^{III} complexes with very low distortion due to the absence of geometric constraints (Figures 2–5). It is worth noting that the Au–P bond lengths of 2.3969 and 2.4067 Å for complex **1** are very close to the bond lengths measured for monomeric complexes with chelating 1,2-*bis*(diphenylphosphino)benzene ligands[31] suggesting that the geometric constraint does not influence the Au–P bond length. For complex **3**, we observe a bending of the bipyridine similarly to what was previously observed for $[(C^C)Au(N^N)]^+$ complexes.[30] As for phosphine containing dimers, similar Au–N bond length are observed for **4** when compared to monomeric complexes with chelating

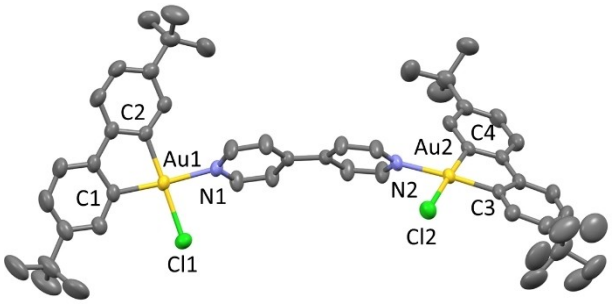

Figure 5. Crystal structure of complex **4**. Ellipsoids set at 50% probability. Hydrogen atoms have been omitted for clarity. Selected bond distances [Å] and angles [°] measured at 200 K: Au_1–Cl_1 2.3721(8), Au_1–N_1 2.130(3), Au_1–C_2 2.025(3), Au_1–C_1 2.029(3), Cl_1–Au_1–N_1 86.49(7), N_1–Au_1–C_2 94.93(11), C_2–Au_1–C_1 81.40(13), C_1–Au_1–Cl_1 96.97(10). By symmetry Au_2 corresponds to Au_1.

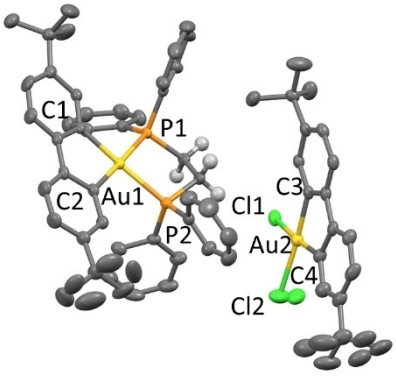

Figure 6. Crystal structure of complex **5**. Ellipsoids set at 50% probability. Some hydrogen atoms and *Me*OH have been omitted for clarity. Selected bond distances [Å] and angles [°] measured at 200 K: Au_1–P_2 2.3741(9), Au_1–P_1 2.3869(9), Au_1–C_1 2.077(3), Au_1–C_2 2.076(3), Au_2–Cl_1 2.3799(10), Au_2–Cl_2 2.390(2), Au_2–C_4 2.032(4), Au_2–C_3 2.033(3), P_2–Au_1–P_1 84.01(3), P_1–Au_1–C_1 97.66(10), C_1–Au_1–C_2 81.09(14), C_2–Au_1–P_2 97.39(10), Cl_1–Au_2–Cl_2 87.24(6), Cl_2–Au_2–C_4 96.40(12), C_4–Au_2–C_3 81.24(15), C_3–Au_2–Cl_1 95.47(10).

bipyridine ligands and for pyridine containing monomeric analog.[28,30]

The crystal structure of digold salt **5** confirmed the proposed [(C^C)Au(P^P)][(C^C)AuCl$_2$] structure supported by NMR data (Figure 6). The crystallographic parameters for the [(C^C)Au(P^P)]$^+$ cation are in very good agreement with those previously measured for the same cation.[31] In the same way, Au–Cl bond lengths in the [(C^C)AuCl2]$^-$ anion are in good agreement with dimeric complexes **1**–**4** and related complexes reported elsewhere[28] although Cl2 is localized onto two positions: Cl2 A major position (90%) and Cl2B minor position (10%).

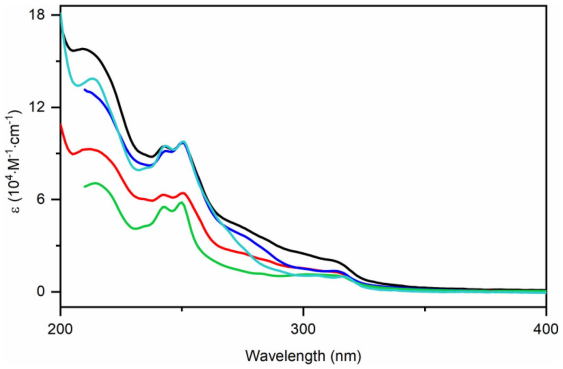

Figure 7. Electronic absorption in dilute (2.0×10^{-5} M) CH_3CN solution for compounds **1** (black), **2** (red), **3** (blue), **4** (green) and **5** (cyan).

Thermal analysis

The thermal properties of all the compounds were assessed by thermogravimetric analysis (TGA) and the corresponding data are plotted in Figures S1–S3 of the Supporting Information. The decomposition temperatures with 5% weight loss ($T_{5\%}$) are 287 °C, 255 °C, 270 °C, 320 °C and 283 °C for compounds **1**, **2**, **3**, **4** and **5**, respectively. For all the compounds, the melting point (T_m) of the pristine microcrystalline powders is above 300 °C, where decomposition starts to be significant. These data show the good thermal stability of these binuclear Au^{III} derivatives.

Photophysical investigation

For all the investigated complexes, absorption and emission spectra were recorded and are displayed in Figures 7–9. The corresponding photophysical data are summarized in Tables 1 and 2.

For all the complexes, the electronic UV-Vis spectra in dilute CH_3CN solution (2.0×10^{-5} M) are characterized by three main absorption regions (Figure 7). At higher energy ($\lambda_{abs} < 230$ nm)

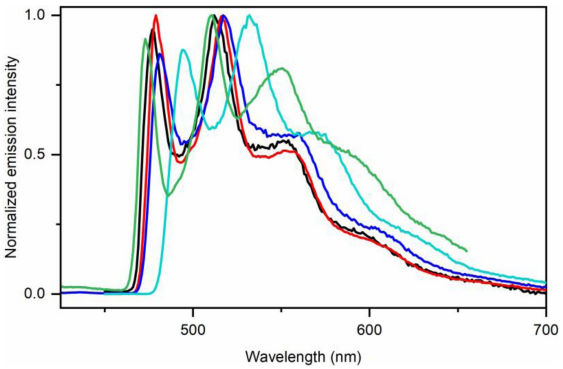

Figure 8. Photoluminescence spectra in 2-MeTHF glassy matrix at 77 K for compounds **1** (black), **2** (red), **3** (blue), **4** (green) and **5** (cyan). Compounds **1**, **2**, **5** were excited at $\lambda_{exc} = 360$ nm; compound **3** was excited at $\lambda_{exc} = 370$ nm and compound **4** was excited at $\lambda_{exc} = 340$ nm.

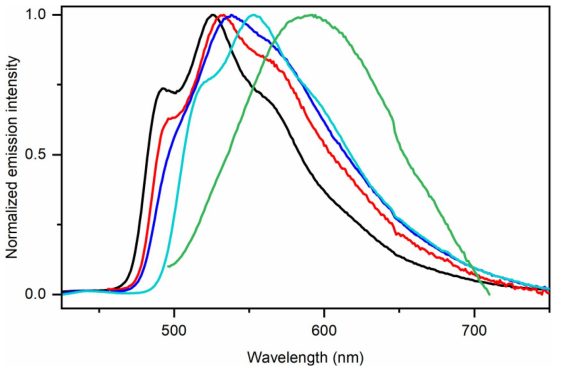

Figure 9. Photoluminescence spectra in the solid state as neat powder for compounds **1** (black), **2** (red), **3** (blue), **4** (green) and **5** (cyan). Compounds **1** and **4** were excited at $\lambda_{exc} = 380$ nm; compounds **2**, **3**, **5** were excited at $\lambda_{exc} = 400$ nm.

Table 1. Photophysical properties of complexes **1**–**5** in dilute CH_3CN solution (2.0×10^{-5} M) at room temperature in air-equilibrated condition and in 2-MeTHF glassy matrix at 77 K.

Compound	λ_{max} (ε) [nm, (10^3 M^{-1} cm^{-1})] room temperature	λ_{em} [nm] 77 K	τ_{obs} [μs]	$\bar{\tau}_{obs}$ [μs]
1	209 (158.1), 243 (94.4), 250 (96.9), 312*sh* (20.4)	477, 514, 556, 596*sh*	137.8	-
2	211 (92.7), 243 (71.0), 250 (72.3), 274*sh* (30.0), 314*sh* (13.9)	479, 517, 558, 599*sh*	126.9	-
3	244 (91.6), 250 (97.2), 275 (36.8), 314 (13.5)	480, 517, 559, 604*sh*	101 (64%) 153.8 (36%)	125.4
4	214 (70.6), 242 (54.9), 250 (58.1), 315 (10.3)	474, 511, 550, 596*sh*	3.91	-
5	213 (138.8), 243 (94.7), 250 (97.1), 316 (10.0)	494, 532, 575, 616*sh*	151 (51%) 100 (49%)	131.2

Table 2. Photophysical properties of complexes **1**–**5** in the solid state at room temperature.

Compound	λ_{em} [nm]	PLQY [%]	τ_{obs} [μs]	$\bar{\tau}_{obs}$ [μs]	k_r [10^3 s^{-1}]	k_{nr} [10^4 s^{-1}]
1	492, 525, 567	6	6.0 (40%) 2.5 (59%)	4.7	12.9	20.1
2	496, 532, 565	1	5.0 (47%) 1.1 (45%)	4.3	2.3	23.2
3	500, 535, 570	1	2.0 (79%) 6.6 (21%)	4.2	2.4	23.7
4	585	1	0.37 (79%) 2.11 (21%)	1.41	7.1	70.2
5	518, 552, 590	6	23.7 (34%) 12.3 (47%) 2.5 (19%)	18.4	3.3	5.1

the transitions involve electronic processes associated with the aryls and heteroaryls of the phosphines (compounds **1**–**3** and **5**) and bipyridine (compound **4**). Moving to lower energy, the 240–250 nm region shows an intense band with $\varepsilon = 5.5$–9.7×10^4 M^{-1} cm^{-1} ascribed to a singlet intraligand (^{1}IL) transition of π–π* nature involving the two cyclometalating biphenyl moieties. Finally, at longer wavelengths ($\lambda_{abs} = 270$–320 nm) the lower intensity band ($\varepsilon = 3.7$–1.0×10^4 M^{-1} cm^{-1}) can be ascribed to a singlet-manifold electronic transition with mainly metal perturbed ligand-to-ligand charge transfer ($^1L_{C\wedge C}L_{bridge}CT$) and ligand-to-metal charge transfer ($^1L_{C\wedge C}MCT$) character, where "C^C" and "bridge" is the biphenyl and the bridging ligand, respectively. These attributions are in agreement with those previously reported on related mononuclear complexes and are further supported by the two-fold increase of their intensity upon dinuclearisation.[29,31]

No emission is detected in fluid solution at room temperature, whereas bluish-green photoluminescence is observed upon lowering the temperature down to 77 K for glassy samples in 2-MeTHF matrix (see Figure 8 and Table 1). For complexes **1**–**3** and **5**, the long-lived nature of the excited state with lifetime values falling in the range $\tau = 100.0$–153.8 μs, along with the highly structured nature of the emission profile strongly support the main ^{3}LC nature of the emitting excited state at low temperature. On the other hand, sizeable increase of the metal-perturbation in the emitting state is accounted for the much shorter excited-state lifetime observed for complex **4** ($\tau = 3.91$ μs).

In the solid state as neat powder, all the dinuclear compounds **1**–**5** display green to yellowish-green photoluminescence with emission maximum peaking between 525 and 552 nm with slightly structured to featureless profile. The corresponding emission spectra are displayed in Figure 9. The emission displays moderate efficiency, with photoluminescence quantum yield (PLQY) in the order 1–6%, with the highest values being observed for derivatives **1** and **5**. These low-to-moderate values are most likely due to the presence of the two monodentate chlorido ligands that provide a high degree of structural flexibility. It hence facilitate detrimental radiationless deactivation pathways as also suggested by the ten- to hundred-fold higher value of the non-radiative rate constant, k_{nr}, compared to the radiative rate, k_r. The value of this latter falls in the 10^3 s^{-1} regime as observed previously for related cationic counterparts and along with the largely unstructured emission profile which points towards a radiative process arising from an excited state with admixed ^{3}LLCT/^{3}LC nature.[31] The ^{3}LLCT character is particularly important for derivative **4** as suggested by the much shorter lifetime ($\tau = 1.41$ μs) observed when compared to derivative **1**–**3** and **5** ($\tau = 4.2$–18.4 μs), and the broader spectral profile (Figure 9).

Computational investigation

Starting from the X-ray crystallographic data, the optimized computed structures agree well with the experimental ones, with a sole exception for compound **5**, as expected (see Table S1–S2 of the Supporting Information. For the latter, which is composed of a soft salt with two different metal complex ions, the calculation well reproduces the structure of each ion. However, with the absence of the solid-state packing, a significant rearrangement of the position of the two units is observed, as exemplified by the Au···Au distance that shortens from 7.470 Å to 6.741 Å when going from the experimental to optimized structure (see Table S2 of Supporting Information). Computational investigation on the [(4,4′-diterbutylbiphenyl)Au(dppe)]$^+$ ion was reported previously by us.[31] Consequently, compound **5** will not be discussed any further.

The computed absorption spectra for complexes **1**–**5** are displayed in Figure 10. The results are qualitatively consistent with the main features of the experimental spectra with maxima calculated between 250–280 nm and absorption starting at

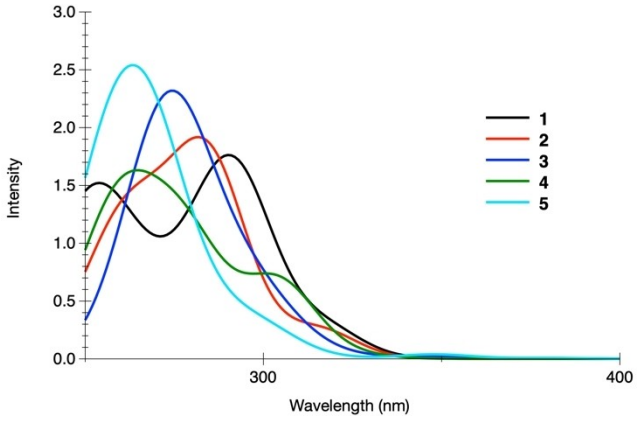

Figure 10. Computed absorption spectra of complexes **1**–**5** in CH_3CN.

about 350 nm. A quantitative agreement is out of reach for these large and flexible molecules due to computational limitations: i) the transitions above 250 nm are not accessible by the calculation because of the high density of excited states (see Tables S4 to S6 Supporting Information); ii) taking into account the number of conformers which contribute to the experimental broad absorption in solution would need tedious and costly molecular dynamics simulations, out of the scope of the present study. For an illustration of conformational effects, Figure S4, of the Supporting Information shows a comparison between the calculated spectra of two energetically close conformers of complex **1**. Moreover, spin-orbit and vibronic effects could aslo modify the fine structure of the calculated spectra.[33] A comparison between scalar and spin-orbit absorption spectra of complex **1** (Figure S4, Supporting Information) indicates that SOC effects are negligible here. Nevertheless, a qualitative assignment of the experimental bands is justified to decipher the broad experimental absorption. All absorption spectra start at around 325 nm (Figure 7 and Figure 10) with intense absorption below 300 nm. The nature of the absorbing states is very similar for complexes **1**, **2** and **3**. The lowest singlet state (S_1) has a mixed $LC_{C\wedge C}/L_{C\wedge C}MCT/L_{C\wedge C}L_{P\wedge P}CT$ character (Figure S5). It can be described as an excitation from the π system of the C^C ligand towards an antibonding σ* orbital located on the gold atoms and the biphenyl, chlorido and phosphine ligand (Figure 11). This σ* orbital is the anticombination of the $d_{x2\text{-}y2}$ gold orbital mixed with binding ligand lone pairs.

Additionally, a contribution of the π-system of the bridging unsaturated ligand (phenyl moiety) is observed for complex **1**. This state is almost degenerate with a second singlet state with similar nature that involves a transition occurring from the other biphenyl π system (not shown). These states are close to the visible domain (394 and 391 nm for **1**, 403 and 399 nm for **2**, 427 and 410 nm for **3**, respectively) but have no intensities. The absorbing singlet states, between 250 and 300 nm, are of same mixed nature with different weight of the three characters in agreement with experimental findings. The lowest T_1 and S_1 states possess similar character (Figure S6). The difference between the three complexes may arise from the delocalization of the accepting orbital as it involves the bridging group: a phenyl in **1**, a double bond in **2** and a triple bond in **3**.

The description is rather different for complex **4**, in which the two gold centers are bridged by the 4,4′-bipyridine ligand. For complex **4**, the lowest S_1 singlet state has an almost pure $L_{C\wedge C}L_{N\wedge N}CT$ character corresponding to electronic excitation from the π system of two C^C ligands towards the π* orbital of the bipyridine (N^N) (Figure 12). This singlet state is nearly degenerate with S_2, which possesses a similar character: S_1 and S_2 are computed at $\lambda = 443$ and 442 nm, respectively. These ^{1}LLCT excited states are significantly stabilized as compared to that of complex **1**. This stabilization of the ^{1}LLCT states in **4**, compared to **1**–**3**, is due to the localization of the LUMO on the bipyridine at −2.979 eV, while the Au-ligands σ* orbital is located much higher in energy, at −2.015 eV. The T_1 state of **4** is of similar character to that of the S_1, a ^{3}LLCT state. At higher energy, the absorption spectrum of **4** is dominated by various charge transfer processes towards the π* orbital of the bipyridine.

The lowest T_1 triplet excited state for each of the four complexes has been fully optimized. For **1**, **2** and **3**, T_1 is electronically localized exclusively on one gold center and its coordination environment, whereas the involvement of the bridging P^P π-system is negligible (Figure 13). The $S_0 \rightarrow T_1$ transition can be described as an electron density displacement from the π-system of one biphenyl towards the σ* Au-ligand orbital. This implies that a degenerate minimum on the lowest triplet potential energy surface (PES) exists. This second

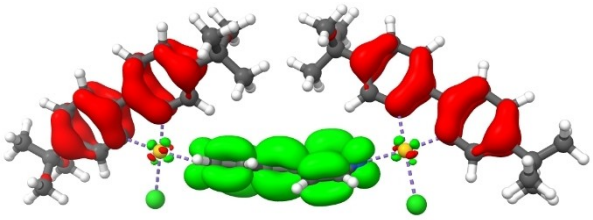

Figure 12. Electron density difference maps between ground and lowest excited singlet state for complex **4**. Electronically depleted and enriched areas are depicted in red and in green, respectively.

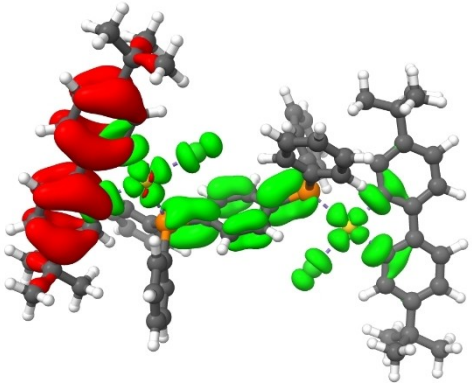

Figure 11. Electron density difference maps between ground and lowest excited singlet state for complex **1**. Electronically depleted and enriched areas are depicted in red and in green, respectively.

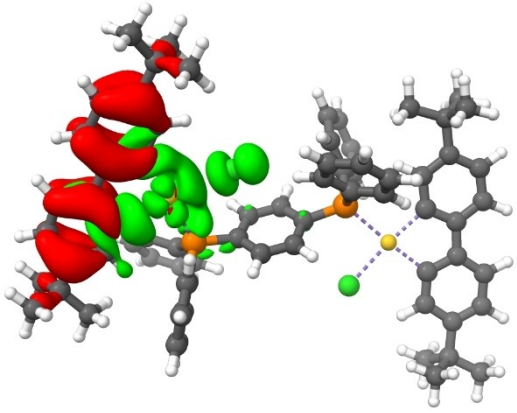

Figure 13. Electron density difference between ground and lowest triplet state of **1** at the optimized triplet state (T_1) geometry. Electronically depleted and enriched areas are depicted in red and in green, respectively.

minimum involves the other biphenyl ligand and gold center. Expectantly, the population of this antibonding σ* orbital leads to significant lengthening of the Au–C and Au–Cl bond distances that are oriented *trans* to each other. As a matter of example, the *d*(Au–Cl) elongates from 2.407 Å to 2.778 Å from the S_0 to T_1 states in complex **1**, yielding to a chloride ligand that is almost de-coordinated (Table S3). This is associated to a pyramidalization of the gold environment with a ∠(C–C–Cl–P) = 206.7° vs. 174.4° found in the S_0 geometry. The structures of the T_1 state of **2** and **3** undergo similar geometrical rearrangements. The computed emission wavelengths for **1**, **2** and **3** are in the range of 700–750 nm (Table S3), markedly different from the experimental values recorded in the solid state. It is indeed reasonable to think that upon photo-excitation and population of the T_1 state, the chloride ligand is probably de-coordinated in solution and allows for the formation of the solvato-complex, opening the way for efficient non-radiative decay. This hypothesis would agree with the absence of emission experimentally observed for samples in dilute CH_3CN solution at room temperature (see above). Upon rigidification of the environment in the solid state and in 2-MeTHF glassy matrix at 77 K, the de-coordination of the chloride anion is unlikely to occur and nuclear distortions are limited, restoring the luminescence via the lowest T_1 electronic state.

The description is different for complex **4**. By optimization of the lowest-lying T_1 state at the ΔSCF level, the LLCT character is retained, and it is ascribed to a charge transfer from the π system of one C^C ligand towards the π* orbital of the bipyridine (Figure 14). This $L_{C^C}L_{N^N}CT$ character of T_1, unique to complex **4**, is consistent with the experimental findings, as **4** behaves differently than the other complexes (Table 2). Furthermore, the small geometric distortions induced by the nature of T_1 state (Table S2) yield a computed emission wavelength that is much closer to the experimental one (658 nm vs 585 nm, respectively, see Table 2 and S2) compared to the computed values for the P^P-based complexes **1**–**3**.

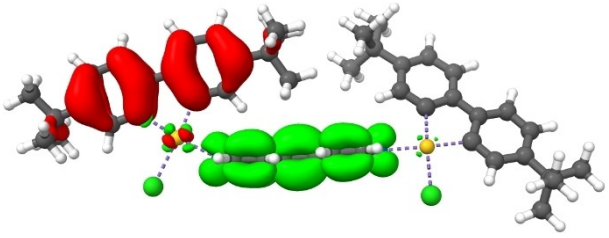

Figure 14. Electron density difference maps between ground and lowest triplet state for complex **4** at the optimized triplet state (T_1) geometry. Electronically depleted and enriched areas are depicted in red and in green, respectively.

Antiproliferative study

All complexes **1**–**5** were screened against lung adenocarcinoma cell line A549 since platinum-based complexes are currently the standard of care for this type of cancer.[34] Evaluation of cell proliferation of A549 cells after 72 h of incubation with complexes **1**–**5** and cisplatin at concentrations of 10 and 1 μM was carried out by using the established MTT assay that consists of the quantification of mitochondrial activity correlated to cell proliferation (see the experimental section for details). The results are depicted in Figure 15.

Among the neutral binuclear complexes, only complex **2** demonstrated a significant inhibition of cell growth leading to 41% of cell viability after treatment with a 10 μM stock solution. Very interestingly, the zwitterionic compound **5** led to a very strong reduction of the cell viability of the cancer cells at both concentrations (0.9% and 14% of remaining cell viability at 10 and 1 μM respectively). As such, compounds **2** and **5** being the most promising were tested against a larger panel of cancer and non-cancerous cells and their median efficient concentration (EC_{50}) were measured (Table 3).

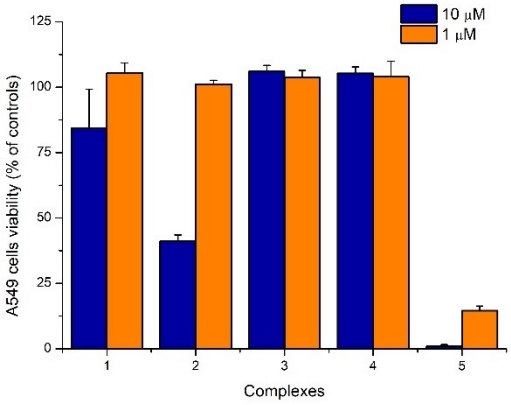

Figure 15. Inhibition of A549 cell growth by complexes **1**–**5**; each data represents the average of three experiments ± standard error.

Table 3. EC_{50} of compounds **2**, **5** and cisplatin on human cancerous and non-cancerous cell lines after 72 h of incubation at 37 °C; each data represents the average of three experiments ± standard error.

Compound	EC_{50} ± sd (μM)			
	A549 (lung)	MDA-MB-231 (breast)	A2780 (ovary)	MCF10 A (non-cancer breast)
2	7.5 ± 1.6	11.3 ± 1.0	7.2 ± 1.5	19 ± 6
5	0.13 ± 0.04	0.20 ± 0.08	0.066 ± 0.003	0.33 ± 0.07
Cisplatin	1.7 ± 0.5	20.4 ± 3.4[a]	1.0 ± 0.2[a]	3.2 ± 0.8[a]

[a] data taken from Ref. [35].

The digold salt **5** demonstrated a very high antiproliferative activity against all tested cell lines with EC_{50} values of 0.13 ± 0.04, 0.13 ± 0.03 and 0.06 ± 0.003 μM against A549, MDA-MB-231 and A2780 cancer cells respectively: an activity that is up to 150 times more potent than the clinically used drug cisplatin. Moreover, it is interesting to note that complex **5** demonstrated a more than two-fold lower antiproliferative activity against the non-cancerous cells MCF10 A. Complex **2** appeared much less potent with EC_{50} values of 7.5 ± 1.6, 10.7 ± 0.2 and 7.2 ± 1.5 μM against A549, MDA-MB-231 and A2780 cancer cells respectively, being thus more active than cisplatin on the "triple negative" breast cancer cells MDA-MB-231. As for **5**, complex **2** appeared more potent on the various tested cancer cell lines than the non-cancerous one.

When tested on the A549 lung cancer cells, the free P^P ligand of complex **2** showed an EC_{50} value of 15.6 ± 4.1 μM suggesting that the observed activity of complex **2** might arise from release of the P^P ligand, as was previously suggested for (C^N^C)-based dimers[21] and for $[(C^C)Au(N^N)]^+$ complexes.[30]

Considering the reported high cytotoxicity of diphosphine ligands,[21] a reactivity study of the cationic fragment of the digold salt **5** with representative biomolecules was carried out and analyzed by electrospray ionization-mass spectrometry ESI-MS). Digold salt **5** was incubated for 24 h at 37 °C in the presence of one equivalent of cysteine, methionine, histidine, serine, guanine and a mixture of one equivalent of each (Figure S7). Interestingly, while related $[(C^C)Au(N^N)]^+$ complexes reacted quantitively with both cysteine and histidine in the same conditions leading to the substitution of the (N^N) ligands by the amino acids,[30] no reaction was observed in any cases for the $[(C^C)Au(P^P)]^+$ cation. Compound **5** was then reacted for 24 h at 37 °C with up to 50 equivalents of GSH, one of the most abundant intracellular reducing agents associated with resistance to cisplatin[36] (Figure 16) and as previously observed with single amino acids no reaction products were detected even at higher concentrations of GSH. Although more investigations are required to characterize the intracellular speciation of the $[(C^C)Au(P^P]^+$ cation, these results seem to suggest that the anticancer activity of **5** might not arise from the toxicity of de-coordinated diphosphine ligand, but rather from the intrinsic activity of the gold fragments.

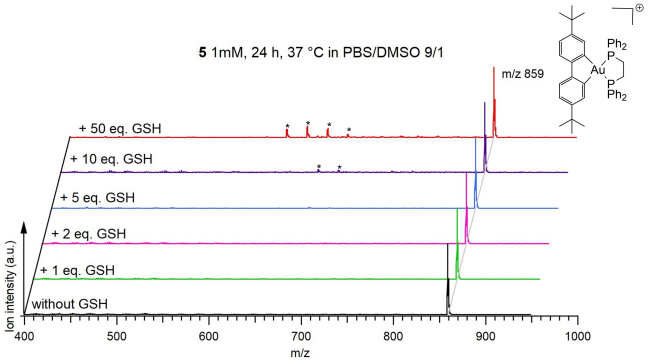

Figure 16. Reactivity of the cation of **5** with GSH (1, 2, 5, 10 and 50 equiv.) for 24 h at 37 °C. Samples were analyzed by ESI-MS. The ions marked with a star on the spectra are attributed to $[GSSG + Na]^+$ (m/z 635.1), $[GSSG–H + 2Na]^+$ (m/z 657.1), $[GSSG\text{-}2H + 3Na]^+$ (m/z 679.1), and $[GSSG\text{-}3H + 4Na]^+$ (m/z 701.1).

Conclusions

We herein report on the synthesis of four neutral Au^{III}-based binuclear compounds bearing either diphosphines or a bipyridine bridging ligand. When the gold precursor [(C^C)AuCl] was allowed to react with 1,2-diphenylphosphinoethane (dppe) in a 2:1 ratio, the reaction led to a digold salt in which the diphosphine chelates the Au^{III} center. This generated a complex salt with a $[(C^C)Au(P^P)]^+$ cation associated with a $[(C^C)AuCl_2]^-$ anion (compound **5**). When the gold precursor was reacted with non-chelating phosphines and 4,4′-bipyridine, binuclear species were obtained where biphosphine or bipyridine acts as a bridging ligand between two Au^{III} centers (compounds **1**–**4**). The structure of all the complexes and the digold salt was assessed in solution by various NMR techniques and in the solid state by X-ray diffraction. The complexes show moderately intense solid-state luminescence in the yellow to green region of the visible spectrum with photoluminescence quantum yields (PLQY) up to 10% for compound **5**, which shifts to the greenish-blue in 2-MeTHF glassy matrix at 77 K. No emission is detectable in fluid solution. The photoluminescence is ascribed to a radiative relaxation with admixed ^{3}LLCT/^{3}LC character, and it is likely highly competitive with radiationless pathways allowed by the flexibility of the two chlorido ligands. Regarding the cytotoxicity studies, the binuclear complex **2** with the *trans*-1,2-dppethylene ligand appeared to be the most potent within the neutral series, showing IC_{50} values in the low μM range. Compound **5** demonstrated very high activities in the nM range, much stronger than cisplatin and associated with reduced activity on non-cancerous cells. Reactivity studies carried out using potentially coordinating biomolecules have not revealed any reactivity of $[(C^C)Au(P^P)]^+$ cation of compound **5** with either the tested amino acids or GSH. These findings extend the scope of diphosphine and bipyridine-based organo-Au^{III} derivatives and highlight their great potential as combined photoluminescent and anticancer agents.

Experimental Section

General remarks

Anhydrous solvents were obtained by standard procedures. Chemicals were purchased from various manufacturers and used as received. ^{1}H, ^{13}C and ^{31}P NMR spectra were acquired with Bruker 300 or 400 MHz spectrometers. Chemical shifts (δ) are expressed as ppm referenced to the solvent residual signal. Splitting patterns are expressed as follows: s, singlet; d, doublet; t, triplet; m, multiplet. HRMS analysis were carried out at the Mass Spectrometry Sciences Sorbonne University (MS^3U) platform of Sorbonne Université (Paris). Elemental analyses were performed at the Service Chromato-Masse Microanalyse of the Université Paris-Saclay (Châtenay-Malabry, France). The dimeric gold precursor has been synthesized according

to reported procedures.[28] Diphosphine ligands have been purchased at Sigma-Aldrich and used as received.

Synthesis of complexes 1–3

In a Schlenk tube under N_2 atmosphere, the gold dimer (40 mg, 0.04 mmol) is suspended into degassed dichloromethane (4 mL). The diphosphine (0.04 mmol) is added and the reaction is kept under N_2 atmosphere at room temperature for 3 h. The reaction mixture is filtered through a glass frit with Celite and the obtained solution is concentrated under reduced pressure. The product is purified by silica column chromatography using a mixture of DCM/cyclohexane (1/1 v/v). After drying, the pure products are obtained as pale yellow powders.

Complex 1: **1,4-diphenylphosphinobenzene** (18 mg): The pure product is obtained as a pale yellow powder (34 mg, 0.023 mmol, 59% yield). ^{1}H NMR ($CDCl_3$, 300 MHz, 300 K): 8.48 (dd, $^4J_{P-H}$ = 9.4 Hz, $^4J_{H-H}$ = 1.7 Hz, 2 H, H^{11}), 7.78–7.84 (m, 8 H, H^{15}), 7.56–7.42 (m, 15 H, $H^{14}+H^{16}+H^{18}$), 7.27–7.34 (m, 4 H, H^5+H^8), 7.20 (dd, $^3J_{H-H}$ = 7.8 Hz, $^4J_{H-H}$ = 1.7 Hz, 2 H, H^9), 7.03 (dd, $^3J_{H-H}$ = 7.9 Hz, $^4J_{H-H}$ = 1.9 Hz, 2 H, H^4), 6.94 (m, 2 H, H^2), 1.35 (s, 18 H, ^{t}Bu), 0.66 (s, 18 H, ^{t}Bu). $^{13}C\{^1H\}$ Jmod NMR ($CDCl_3$, 75.5 MHz, 300 K): δ 166.4 (d, $^3J_{P-C}$ = 128.3 Hz, C^7), 154.5 (m, C^6), 151.6 (m, C^1), 150.0 (m, C^{10}), 149.6 (s, C^3), 149.2 (s, C^{12}), 135.8 (m, C^{15}), 134.3 (t, $^2J_{P-C}$ = 10.7 Hz, C^2+C^{18}), 133,7 (d, $^1J_{P-C}$ = 48.7 Hz, C^{17}), 132.4 (s, C^{16}), 130.6 (s, C^{11}), 129.3 (m, C^{14}), 127.1 (d, $^1J_{P-C}$ = 47.6 Hz, C^{13}), 124.8 (s, C^9), 124.1 (s, C^4), 121.2 (s, $C^{5/8}$), 120.8 (m, $C^{5/8}$), 35.6 (s, $C_{quat.tBu}$), 34.6 (s, $C_{quat.tBu}$), 31.6 (s, $CH_{3\text{-}tBu}$), 30.9 (s, $CH_{3\text{-}tBu}$). $^{31}P\{^1H\}$ NMR ($CDCl_3$, 121.5 MHz, 300 K): δ 42.1 (s, 2 P, P–Au). ESI-MS (MeCN) *positive mode exact mass for* $[C_{70}H_{72}P_2AuCl]^+$ (1403.4123): measured *m/z* 1403.4139 $[M-Cl]^+$. Calcd for $C_{70}H_{72}P_2Au_2Cl_2$ (1440.13): C, 58.38; H, 5.04. Found: C, 58.70; H 4.54.

Complex 2: ***trans*-1,2-bis(diphenylphosphino)ethylene** (16 mg): The pure product is obtained as a pale yellow powder (40 mg, 0.029 mmol, 72% yield). ^{1}H NMR ($CDCl_3$, 300 MHz, 300 K): δ 8.43 (dd, $^4J_{P-H}$ = 9.7 Hz, $^4J_{H-H}$ = 1.9 Hz, 2 H, H^{11}), 7.94–8.00 (m, 8 H, H^{15}), 7.46–7.56 (m, 12 H, $H^{14}+H^{16}$), 7.27–7.31 (m, 4 H, H^5+H^8), 7.21 (dd, $^3J_{H-H}$ = 8.1 Hz, $^4J_{H-H}$ = 1.9 Hz, 2 H, H^9), 7.02 (d, $^3J_{H-H}$ = 8.1 Hz, $^4J_{H-H}$ = 1.9 Hz, 2 H, H^4), 6.93 (m, 2 H, H^2), 6.66 (t, $^2J_{H-H}$ = 21.6 Hz, 2 H, H^{17}), 1.40 (s, 18 H, ^{t}Bu), 0.65 (s, 18 H, ^{t}Bu). $^{13}C\{^1H\}$ Jmod NMR ($CDCl_3$, 75.5 MHz, 300 K): δ 166.2 (d, $^3J_{P-C}$ = 128.4 Hz, C^7), 154.2 (t, $^3J_{P-C}$ = 3.7 Hz, C^6), 151.4 (t, $^2J_{P-C}$ = 2.2 Hz, C^1), 149.9 (t, $^4J_{P-C}$ = 4.5 Hz, C^{10}), 149.6 (s, C^3+C^{12}), 138.2 (d, $^1J_{P-C}$ = 37.8 Hz, C^{17}), 135.9 (t, $^3J_{P-C}$ = 6.1 Hz, C^{15}), 134.1 (t, $^3J_{P-C}$ = 5.3 Hz, C^2), 132.8 (s, C^{16}), 129.7 (m, C^{14}), 129.5 (s, C^{11}), 124.9 (s, C^9), 124.2 (s, C^4), 123.9 (dd, $^1J_{P-C}$ = 46.5 Hz, $^2J_{P-C}$ = 12.1 Hz, $C^{12}+C^{13}$), 121.3 (s, C^8), 120.9 (t, $^4J_{P-C}$ = 3.7 Hz, C^5), 35.6 (s, $C_{quat.tBu}$), 34.6 (s, $C_{quat.tBu}$), 31.7 (s, $CH_{3\text{-}tBu}$), 30.8 (s, $CH_{3\text{-}tBu}$). $^{31}P\{^1H\}$ NMR ($CDCl_3$, 121.5 MHz, 300 K): δ 34.7 (s, 2 P, P–Au). ESI-MS (MeCN) *positive mode exact mass for* $[C_{66}H_{71}P_2AuCl_2]^+$ (1389.3734): measured *m/z* 1389.3786 $[M+H]^+$. Calcd for $C_{70}H_{72}P_2Au_2Cl_2.6H_2O$ (1498.16): C, 52.91; H, 5.52. Found: C, 52.95; H 5.14.

Complex 3: **1,2-bis(diphenylphosphino)-acetylene** (16 mg): The pure product is obtained as a pale yellow powder (29 mg, 0.019 mmol, 52% yield). ^{1}H NMR ($CDCl_3$, 300 MHz, 300 K): δ 8.37 (d, $^4J_{P-H}$ = 10.5 Hz, 2 H, H^{11}), 7.60–7.67 (m, 8 H, $H_{ortho-Ph}$), 7.47–7.52 (m, 4 H, $H_{para-Ph}$), 7.32–7.39 (m, 10 H, $H^{5/8}+H_{meta-Ph}$), 7.29 (d, $^3J_{H-H}$ = 7.9 Hz, 2 H, $H^{5/8}$), 7.21 (d, $^3J_{H-H}$ = 8.1 Hz, 2 H, H^9), 7.06–7.11 (m, 4 H, H^2+H^4), 1.34 (s, 18 H, ^{t}Bu), 0.66 (s, 18 H, ^{t}Bu). $^{13}C\{^1H\}$ Jmod NMR ($CDCl_3$, 75.5 MHz, 300 K): δ 166.5 (d, $^3J_{P-C}$ = 131.4 Hz, C^7), 155.3 (d, $^3J_{P-C}$ = 8.4 Hz, C^6), 151.1 (d, $^2J_{P-C}$ = 5.0 Hz, C^1), 150.2 (d, $^4J_{P-C}$ = 2.8 Hz, C^3), 150.0 (d, $^4J_{P-C}$ = 8.9 Hz, C^{10}), 149.4 (s, C^{12}), 134.2 (d, $^2J_{P-C}$ = 13.5 Hz, $C_{ortho-Ph}$), 132.6 (d, $^4J_{P-C}$ = 2.8 Hz, $C_{para-Ph}$), 132.1 (d, $^3J_{P-C}$ = 11.3 Hz, C^2), 130.3 (s, C^{11}), 129.5 (d, $^3J_{P-C}$ = 12.9 Hz, $C_{meta-Ph}$), 125.4 (d, $^1J_{P-C}$ = 54.2 Hz, $C_{ipso-Ph}$), 125.0 (s, C^9), 124.7 (s, C^4), 124.5 (s, C^5), 120.9 (d, $^4J_{P-C}$ = 8.9 Hz, C^5), 102.2 (dd, $^1J_{P-C}$ = 75.5 Hz, $^2J_{P-C}$ = 3.3 Hz, C^{13}), 35.6 (s, $C_{quat.tBu}$), 34.7 (s, $C_{quat.tBu}$), 31.5 (s, $CH_{3,tBu}$), 31.1 (s, $CH_{3,tBu}$). $^{31}P\{^1H\}$ NMR ($CDCl_3$, 121.5 MHz, 300 K): δ 20.0 (s, 2 P, P–Au). Although various ionisation methods were tested, no HRMS detection of the molecular ion could be achieved. Calcd for $C_{66}H_{68}P_2Au_2Cl_2$ (1388.05): C, 57.11; H, 4.94. Found: C, 57.06; H 5.30.

Synthesis of complex 4

In a round-bottom flask, the gold dimer (50 mg, 0.05 mmol) is suspended into dichloromethane (5 mL). **4,4′-bipyridine** (8 mg, 0.05 mmol) is added and the reaction is kept at room temperature for 2 h. The reaction mixture is filtered through a glass frit with Celite and the obtained solution is concentrated under reduced pressure. Upon addition of a large amount of petroleum ether, a pale yellow precipitate is formed which is recovered and yields after drying the pure product as a yellow powder (39 mg, 0.034 mmol, 68% yield). ^{1}H NMR (CD_2Cl_2, 300 MHz, 300 K): δ 9.10 (d, $^3J_{H-H}$ = 6.3 Hz, 4 H, H^{13}), 8.15 (d, $^4J_{H-H}$ = 1.7 Hz, 2 H, H^{11}), 8.08 (d, $^3J_{H-H}$ = 6.3 Hz, 4 H, H^{14}), 7.31 (d, $^3J_{H-H}$ = 8.04 Hz, 2 H, $H^{5/8}$), 7.21–7.27 (m, 6 H, $H^4+H^9+H^{5/8}$), 6.49 (d, $^4J_{H-H}$ = 1.7 Hz, 2 H, H^2), 1.35 (s, 18 H, ^{t}Bu), 1.14 (s, 18 H, ^{t}Bu). Due to low solubility, no ^{13}C NMR spectrum could be recorded. ESI-MS (MeCN) positive mode exact mass for $[C_{50}H_{57}N_2Au_2Cl_2]^+$ (1149.3224): measured m/*z* 1149.3236 $[M+H]^+$. Calcd for $C_{50}H_{56}N_2Au_2Cl_2.2H_2O$ (1185.88): C, 50.64; H, 5.10; N, 2.36. Found: C, 50.99; H 5.11; N, 2.34.

Synthesis of complex 5

In a Schlenk tube under N_2 atmosphere, the gold dimer (40 mg, 0.04 mmol) is suspended into degassed dichloromethane (4 mL). **1,2-bis(diphenylphosphino)ethane** (16 mg, 0.04 mmol) is added and the reaction is kept under N_2 atmosphere at room temperature for 3 h. The reaction mixture is filtered through a glass frit with Celite and the obtained solution is concentrated under reduced pressure. Upon addition of a large amount of petroleum ether, a pale-yellow precipitate is formed which is recovered and yields after drying the pure product as a pale yellow powder (50 mg, 0.036 mmol, 89% yield). ^{1}H NMR ($CDCl_3$, 300 MHz, 300 K): δ 8.30 (s, 2 H, H^9), 7.76–7.83 (m, 8 H, $H_{ortho-Ph}$), 7.55–760 (m, 4 H, $H_{para-Ph}$), 7.46–7.51 (m, 8 H, $H_{meta-Ph}$), 7.39 (dd, $^3J_{H-H}$ = 7.7 Hz, $^5J_{P-H}$ = 3.4 Hz, 2 H, H^5), 7.28 (m, 2 H, H^2), 7.11–7.15 (m, 4 H, H^4+H^{12}), 7.04 (d, $^3J_{H-H}$ = 7.8 Hz, 2 H, H^{11}), 3.15 (dm, $^2J_{P-H}$ = 19.0 Hz, 4 H, H^7), 1.22 (s, 18 H, ^{t}Bu), 0.73 (s, 18 H, ^{t}Bu). $^{13}C\{^1H\}$ Jmod NMR ($CDCl_3$, 75.5 MHz, 300 Hz): δ 162.9 (d, $^3J_{P-C}$ = 112.2 Hz, $^3J_{P-C}$ = 6.7 Hz, C^6), 156.2 (s, C^{13}), 152.1 (m, C^1), 151.0 (s, C^3), 149.4 (s, C^8), 149.0 (s, C^{10}), 136.6 (m, C^2), 134.2 (m, $C_{ortho-Ph}$), 133.6 (s, $C_{para-Ph}$), 130.4 (m, $C_{meta-Ph}+C^9$), 125.2 (s, C^4), 123.6 (s, C^{11}), 123.2 (d, $^1J_{P-C}$ = 51.1 Hz, $C_{ipso-Ph}$), 121.7 (m, C^5), 120.1 (s, C^{12}), 35.2 (s, $C_{quat.tBu}$), 34.7 (s, $C_{quat.tBu}$), 31.6 (s, $CH_{3\text{-}tBu}$), 30.9 (s, $CH_{3\text{-}tBu}$), 29.8 (dd, $^1J_{P-C}$ = 36.2 Hz, $^2J_{P-C}$ = 6.8 Hz, C^7). $^{31}P\{^1H\}$ NMR ($CDCl_3$, 121.5 MHz): δ 59.7 (s, 2 P, P–Au). ESI-MS (MeCN) positive mode exact mass for $[C_{46}H_{48}P_2Au]^+$ (859.2891): measured m/*z* 859.2896 $[M-[(C\text{^}C)AuCl_2]]^+$. Calcd for $C_{66}H_{72}P_2Au_2Cl_2$ (1392.08): C, 56.95; H, 5.21. Found: C, 57.22; H 6.39.

X-ray crystal structure determination

Single crystals were selected, mounted onto a cryoloop and transferred into a cold nitrogen gas stream. Intensity data were collected with a Bruker Kappa-APEX2 CCD diffractometer using micro-source CuKα radiation (**1**–**4**) or a graphite-monochromated MoKα radiation (**5**). Data collection, unit-cell parameters determination, integration and data reduction were performed with the Bruker APEXIII/SAINT[37] suite at 200 K. The structures were solved with SHELXT[38] and refined anisotropically by full-matrix least-squares methods with SHELXL[39] using Olex2.[40]

Molecules form large void areas in the crystal lattice of **3**. In these areas, unattributed residual electron density is present. It should be due to very disordered solvent molecules. A PLATON SQUEEZE[41] procedure was applied on structure refinement to mask electron density of these very disordered solvent regions. Crystals were obtained with a mixture of solvents, so it is impossible to identify and quantify which one are present in the crystal. So, dichloromethane and/or petroleum ether molecules could be present in the crystal lattice.

Deposition Number(s) 2227044 (for **1**), 2227045 (for **2**), 2227046 (for **3**), 2227047 (for **4**), 2227048 (for **5**) contain(s) the supplementary crystallographic data for this paper. These data are provided free of charge by the joint Cambridge Crystallographic Data Centre and Fachinformationszentrum Karlsruhe Access Structures service.

Photophysics

Instrument details. Absorption spectra of fluid solution samples were measured on a Varian Cary 100 double-beam UV-VIS spectrophotometer and baseline corrected. Steady-state emission spectra were recorded on a Horiba Jobin-Yvon IBH FL-322 Fluorolog 3 spectrometer equipped with a 450 W xenon arc lamp, double-grating excitation, and emission monochromators (2.1 nm mm^{-1} of dispersion; 1200 grooves mm^{-1}) and a Hamamatsu R13456 red sensitive Peltier-cooled PMT detector. Emission and excitation spectra were corrected for source intensity (lamp and grating) and emission spectral response (detector and grating) by standard correction curves. Time-resolved measurements were performed using either the time-correlated single-photon counting (TCSPC) or the Multi Channel Scaling (MCS) electronics option of the TimeHarp 260 board installed on a PicoQuant FluoTime 300 fluorimeter (PicoQuant GmbH, Germany), equipped with a PDL 820 laser pulse driver. A pulsed laser diode LDH–P-C-375 ($\lambda = 375$ nm, pulse full width at half maximum FWHM < 40 ps) or LDH–P-C-440B ($\lambda =$ 440 nm, pulse full width at half maximum FWHM < 80 ps) driven at repetition rate in the range 50 kHz–40 MHz) was used to excite the sample either with either single pulse or burst mode. Excitation source was mounted directly on the sample chamber at 90°. The photons were collected by a PMA Hybrid-07 single photon counting detector. The data were acquired by using the commercially available software EasyTau II (PicoQuant GmbH, Germany), while data analysis was performed using the built-in software FluoFit (PicoQuant GmbH, Germany). All the PLQYs on samples were recorded at a fixed excitation wavelength by using a Hamamatsu Photonics absolute PLQY measurements system Quantaurus QY equipped with CW Xenon light source (150 W), monochromator, integrating sphere, C7473 photonics multi-channel analyzer and employing the commercially available U6039–05 PLQY measurement software (Hamamatsu Photonics Ltd., Shizuoka, Japan). All measurements were repeated five times at the excitation wavelength $\lambda_{exc} = 360$ nm, unless otherwise stated.

Methods. For time resolved measurements, data fitting was performed by employing the maximum likelihood estimation (MLE) methods and the quality of the fit was assessed by inspection of the reduced χ^2 function and of the weighted residuals. For multi-exponential decays, the intensity, namely I*(t)*, has been assumed to decay as the sum of individual single exponential decays (Eq. (1)):

$$I(t) = \sum_{i=1}^{n} \alpha_i exp\left(-\frac{t}{\tau_i}\right) \quad (1)$$

where τ_i are the decay times and α_i are the amplitude of the component at $t = 0$. In the tables, the percentages to the pre-exponential factors, α_i, are listed upon normalization. Intensity average lifetimes were calculated by using the following equation (Eq. (2)):

$$\bar{\tau} = \frac{a_1\tau_1^2 + a_2\tau_2^2}{a_1\tau_1 + a_2\tau_2} \quad (2)$$

All the solvents employed were Merck Uvasol® spectrophotometric grade. Deaerated samples were prepared by the freeze-pump-thaw technique by using a custom quartz cuvette equipped with a Rotaflo® stopcock.

Thermal analysis

Thermogravimetric analyses were carried out on a Q50 systems from TA Instruments under air with a thermal scanning rate of 5 °C min^{-1}.

Computational details

All calculations have been performed with ADF 2019[42] at DFT level of theory (B3LYP functional[43]) with Grimme's dispersion corrections.[44] Scalar relativistic effects were taken into account through ZORA Hamiltonian.[45] All atom were described by DZP slater type basis set except the gold cation which was described by TZP basis set.[46] Acetonitrile solvent effect was introduced by the COSMO model.[47] All geometries were fully optimized and absorption spectra were computed by means of TD-DFT on optimized structures. The lowest triplet states were optimized by means of TD-DFT in the same conditions and the emission wavelength extracted from these calculations. The nature of the excited states was determined either by electron density difference between ground and excited state using DGrid package[48] or by THEODore analysis.[49]

Cell culture and cell growth inhibition

Human lung adenocarcinoma cell line A549 and human breast cancer cell lines MDA-MB-231 were cultivated in DMEM (Dulbecco's Modified Eagle Medium) containing GlutaMax I supplemented with 10% FBS and human ovarian adenocarcinoma cells A2780 were cultivated in RPMI1640 medium containing GlutaMax I supplemented with 10% FBS at 37 °C in a humidified atmosphere and 5% CO_2. Non-cancerous cell line MCF10 A was maintained in DMEM:F12 (1:1) cell culture media, 5% heat inactivated horse serum, supplemented with HEPES (20 mM), L-glutamine (2 mM), epidermal growth factor (20 ng/mL), hydrocortisone (500 ng/mL), cholera toxin (100 ng/mL), and insulin (10 μg/mL). Cell viability was evaluated by using a colorimetric method based on the tetrazolium salt [3-(4,5-dimethylthiazol-2-yl)-2,5-diphenyltetrazolium bromide] (MTT), which is reduced by viable cells to yield purple formazan crystals. Cells were seeded in 96-well plates at a density of 40000 cells/mL (100 μL per well). After overnight attachment, a dilution series of the compounds were added in the medium, and cells were incubated for a further 72 h. Stock solutions of the complexes were prepared in water for cisplatin and the bimetallic compounds in DMSO. The percentage of DMSO in the culture medium did not exceed 1%. After 72 h, the medium was removed, and the cells were incubated with MTT solution in PBS (10 μL of a 5 mg/mL) for 2–3 h of incubation. The formed purple formazan crystals were dissolved in 100 μL DMSO by thorough shaking, and the absorbance at 560 nm was read using a microplate reader (FLUOstar OPTIMA, BMG Labtech). Each test was performed with at least 3 replicates and repeated at least 3 times. The IC_{50} value is determined using GraphPad Prism 8.0 software.

Reactivity with biomolecules

Reaction with amino acids and guanine: Stock solutions of compound 5 (20 mM in DMSO) and each amino acid (100 mM in DMSO) were prepared separately. For the reactions with one amino acid or guanine, a mixture of the solution of compound 5 with each amino acid or guanine was made: 250 μL of solution of 5, 50 μL of solution of amino acid or guanine and 200 μL of DMSO. For the reaction of 5 with the mixture of all amino acids and guanine, the following mixture was made: 250 μL of solution of 5 and 50 μL of solution of each amino acid and guanine. This leads to solution of 10 mM of 5 with one equivalent of amino acid and guanine. Solutions were incubated at 37 °C for 24 h and were diluted to 100 μM with MeOH.

Reaction with glutathione: Two stock solutions of glutathione (GSH) were prepared. S_0 at 200 mM in PBS (30.7 mg of GSH dissolved in 500 μL PBS) and S_1 at 20 mM (50 μL of S_0 + 450 μL of PBS). The same solution of complex 5 at 20 mM in DMSO was used. Following this, six solutions, with respectively 0, 1, 2, 5, 10 and 50 equivalents of glutathione and a constant concentration of 5 (10 mM) in a total volume of solution of 200 μL were prepared. After a 24-hour incubation at 37 °C, the solutions were diluted 100 times in methanol for analysis by low resolution mass spectrometry.

Low resolution mass spectrometry experiments were performed using a modified Quattro II mass spectrometer (Micromass, Manchester, U.K.) equipped with an electrospray (ESI) source. The sample solutions were infused into the ESI source at a flow rate of ca. 400 $\mu L \cdot h^{-1}$. The following source parameters were applied: in the positive ion mode ESI capillary voltage 3.50 kV, cone voltage 30 V. Nitrogen was used as the desolvatation and nebulizing gas. The source and desolvatation temperatures were both kept at 100 °C. The data was acquired and analyzed using Masslynx software (version 4.2).

Acknowledgements

Sorbonne Université, the Université de Strasbourg and the CNRS are kindly acknowledged for financial support. M.M. gratefully acknowledges the French Agence Nationale de Recherche (ANR) for funding the grant ANR-21-CE29-0015 "ChirON". B.B. thanks the MS3U plateform for the HR-MS analyses. C.G. thanks the computing center of the Université de Strasbourg for computing time. Dr. Benoît Heinrich is kindly acknowledged for the technical help with TGA analyses. V.G. thanks the College Doctoral of the Université de Strasbourg for partially funding his PhD fellowship. Robin Fleischel of the UFR de Mathématique et d'Informatique of the Université de Strasbourg is kindly acknowledged for help with coding and data processing.

Conflict of Interests

The authors declare no conflict of interest.

Data Availability Statement

The data that support the findings of this study are available from the corresponding author upon reasonable request.

Keywords: antitumor agents · cytotoxicity · gold · luminescence · medicinal chemistry

[1] R. Kumar, C. Nevado, *Angew. Chem. Int. Ed.* **2017**, *56*, 1994–2015.
[2] M. Joost, A. Amgoune, D. Bourissou, *Angew. Chem. Int. Ed.* **2015**, *54*, 15022–15045.
[3] Y. Lu, X. Ma, X. Chang, Z. Liang, L. Lv, M. Shan, Q. Lu, Z. Wen, R. Gust, W. Liu, *Chem. Soc. Rev.* **2022**, *51*, 5518–5556.
[4] R. Malmberg, K. Venkatesan, *Coord. Chem. Rev.* **2021**, *449*, 214182.
[5] G. Moreno-Alcántar, P. Picchetti, A. Casini, *Angew. Chem. Int. Ed.* **2023**, *62*, e202218000.
[6] C. Bronner, O. S. Wenger, *Dalton Trans.* **2011**, *40*, 12409.
[7] B. Bertrand, A. Casini, *Dalton Trans.* **2014**, *43*, 4209–4219.
[8] J. A. Garg, O. Blacque, K. Venkatesan, *Inorg. Chem.* **2011**, *50*, 5430–5441.
[9] M. R. M. Williams, B. Bertrand, D. L. Hughes, Z. A. E. Waller, C. Schmidt, I. Ott, M. O'Connell, M. Searcey, M. Bochmann, *Metallomics* **2018**, *10*, 1655–1666.
[10] J. A. Garg, O. Blacque, T. Fox, K. Venkatesan, *Inorg. Chem.* **2010**, *49*, 11463–11472.
[11] S. Gukathasan, S. Parkin, S. G. Awuah, *Inorg. Chem.* **2019**, *58*, 9326–9340.
[12] J. Hyun Kim, S. Ofori, R. T. Mertens, S. Parkin, S. G. Awuah, *ChemMedChem* **2021**, *16*, 3222–3230.
[13] S. Carboni, A. Zucca, S. Stoccoro, L. Maiore, M. Arca, F. Ortu, C. Artner, B. K. Keppler, S. M. Meier-Menches, A. Casini, M. A. Cinellu, *Inorg. Chem.* **2018**, *57*, 14852–14865.
[14] R. Kumar, A. Linden, C. Nevado, *Angew. Chem. Int. Ed.* **2015**, *127*, 14495–14498.
[15] K. M.-C. Wong, L.-L. Hung, W. H. Lam, N. Zhu, V. W.-W. Yam, *J. Am. Chem. Soc.* **2007**, *129*, 4350–4365.
[16] V. K.-M. Au, K. M.-C. Wong, N. Zhu, V. W.-W. Yam, *J. Am. Chem. Soc.* **2009**, *131*, 9076–9085.
[17] J.-J. Zhang, K.-M. Ng, C.-N. Lok, R. W.-Y. Sun, C.-M. Che, *Chem. Commun.* **2013**, *49*, 5153.
[18] S. K. Fung, T. Zou, B. Cao, P.-Y. Lee, Y. M. E. Fung, D. Hu, C.-N. Lok, C.-M. Che, *Angew. Chem. Int. Ed.* **2017**, 6.
[19] B. Bertrand, J. Fernandez-Cestau, J. Angulo, M. M. D. Cominetti, Z. A. E. Waller, M. Searcey, M. A. O'Connell, M. Bochmann, *Inorg. Chem.* **2017**, *56*, 5728–5740.
[20] J. Fernandez-Cestau, B. Bertrand, M. Blaya, G. A. Jones, T. J. Penfold, M. Bochmann, *Chem. Commun.* **2015**, *51*, 16629–16632.
[21] C. K.-L. Li, R. W.-Y. Sun, S. C.-F. Kui, N. Zhu, C.-M. Che, *Chem. Eur. J.* **2006**, *12*, 5253–5266.
[22] R. W.-Y. Sun, C.-N. Lok, T. T.-H. Fong, C. K.-L. Li, Z. F. Yang, T. Zou, A. F.-M. Siu, C.-M. Che, *Chem. Sci.* **2013**, *4*, 1979.
[23] J. H. Kim, E. Reeder, S. Parkin, S. G. Awuah, *Sci. Rep.* **2019**, *9*, 12335.
[24] C. Olelewe, J. H. Kim, S. Ofori, R. T. Mertens, S. Gukathasan, S. G. Awuah, *iScience* **2022**, *25*, 104340.
[25] I. Chambrier, D. L. Hughes, R. J. Jeans, A. J. Welch, P. H. M. Budzelaar, M. Bochmann, *Chem. Eur. J.* **2020**, *26*, 939–947.
[26] A. Zeineddine, L. Estévez, S. Mallet-Ladeira, K. Miqueu, A. Amgoune, D. Bourissou, *Nat. Commun.* **2017**, *8*, 565.
[27] J. P. Reid, M. Hu, S. Ito, B. Huang, C. M. Hong, H. Xiang, M. S. Sigman, F. D. Toste, *Chem. Sci.* **2020**, *11*, 6450–6456.
[28] B. David, U. Monkowius, J. Rust, C. W. Lehmann, L. Hyzak, F. Mohr, *Dalton Trans.* **2014**, *43*, 11059–11066.
[29] K. T. Chan, G. S. M. Tong, Q. Wan, G. Cheng, C. Yang, C.-M. Che, *Chemistry* **2017**, *12*, 2104–2120.
[30] S. Khodjoyan, E. Remadna, H. Dossmann, D. Lesage, G. Gontard, J. Forté, H. Hoffmeister, U. Basu, I. Ott, P. Spence, Z. A. E. Waller, M. Salmain, B. Bertrand, *Chem. Eur. J.* **2021**, *27*, 15773–15785.
[31] J. Yang, V. Giuso, M.-C. Hou, E. Remadna, J. Forté, H.-C. Su, C. Gourlaouen, M. Mauro, B. Bertrand, *Inorg. Chem.* **2023**, *62*, 4903–4921.
[32] I. Chambrier, L. Rocchigiani, D. L. Hughes, P. M. H. Budzelaar, M. Bochmann, *Chem. Eur. J.* **2018**, *24*, 11467–11474.
[33] S. Mandal, C. Daniel, *Phys. Chem. Chem. Phys.* **2023**, *25*, 18720–18727.
[34] H. Lemjabbar-Alaoui, O. U. Hassan, Y.-W. Yang, P. Buchanan, *Biochim. Biophys. Acta Rev. Cancer* **2015**, *1856*, 189–210.
[35] B. Bertrand, C. Botuha, J. Forté, H. Dossmann, M. Salmain, *Chem. Eur. J.* **2020**, *26*, 12846–12861.
[36] H. H. W. Chen, M. T. Kuo, *Met.-Based Drugs* **2010**, *2010*, 1–7.
[37] Bruker, Bruker AXS Inc., Madison, Wisconsin, USA, **2012**.
[38] G. M. Sheldrick, *Acta Crystallogr. Sect. A* **2015**, *71*, 3–8.
[39] G. M. Sheldrick, *Acta Crystallogr. Sect. C* **2015**, *71*, 3–8.

[40] O. V. Dolomanov, L. J. Bourhis, R. J. Gildea, J. A. K. Howard, H. Puschmann, *J. Appl. Crystallogr.* **2009**, *42*, 339–341.
[41] A. L. Spek, *Acta Crystallogr. Sect. C* **2015**, *71*, 9–18.
[42] G. te Velde, F. M. Bickelhaupt, E. J. Baerends, C. Fonseca Guerra, S. J. A. van Gisbergen, J. G. Snijders, T. Ziegler, *J. Comput. Chem.* **2001**, *22*, 931–967.
[43] P. J. Stephens, F. J. Devlin, C. F. Chabalowski, M. J. Frisch, *J. Phys. Chem.* **1994**, *98*, 11623–11627.
[44] S. Grimme, J. Antony, S. Ehrlich, H. Krieg, *J. Chem. Phys.* **2010**, *132*, 154104.
[45] E. van Lenthe, A. Ehlers, E.-J. Baerends, *J. Chem. Phys.* **1999**, *110*, 8943–8953.
[46] E. van Lenthe, E. J. Baerends, *J. Comput. Chem.* **2003**, *24*, 1142–1156.
[47] C. C. Pye, T. Ziegler, *Theor. Chem. Acc.* **1999**, *101*, 396–408.
[48] K. D. Kobout, DGRID, version 4.6, Max Planck Society, Radebeul, Germany, **2011**.
[49] F. Plasser, *J. Chem. Phys.* **2020**, *152*, 084108.

Manuscript received: June 23, 2023
Revised manuscript received: August 22, 2023
Accepted manuscript online: August 23, 2023
Version of record online: ■■, ■■

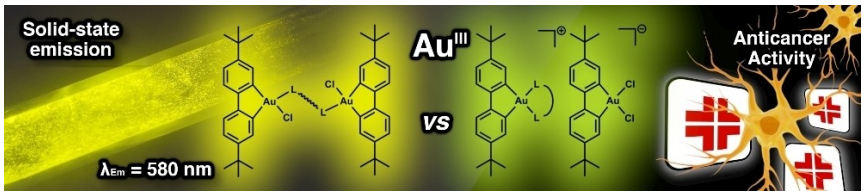

Four binuclear Au(III) complexes have been synthetized using non-chelating bidentate ligands. When a chelating ligand was used, a digold salt was obtained resulting from the chelation of the diphosphine ligand on one Au moiety and a $[(C^C)AuCl_2]^-$ anion. The complexes appeared strongly emissive in solid state and the digold salt presented anticancer activities in the nanomolar range with no modification of the $[(C^C)Au(P^P)]^+$ in the presence of biomolecules.

V. Giuso, J. Yang, J. Forté, H. Dossmann, Dr. C. Daniel, Dr. C. Gourlaouen, Dr. M. Mauro, Dr. B. Bertrand**

1 – 13

Binuclear Biphenyl Organogold(III) Complexes: Synthesis, Photophysical and Theoretical Investigation, and Anticancer Activity